ENGINEERING Transformative Materials
https://doi.org/10.2738/ENGTM.2026.0008

Research Articles

Deep Learning-Empowered Inverse Design of Metasurfaces for Tailored Superchiral Fields and Enhanced Chiral Sensing

Yongliang Li[1*], Chengdong Tao[2*], Zhenggang Pan[1], Xingwen Tang[1], Yan Li[3], Ji Zhou[2,4], Chuanbao Liu (✉)[1], Yang Bai (✉)[1]

1 Beijing Key Laboratory of Materials Intelligent Technology, Institute for Advanced Materials and Technology, University of Science and Technology Beijing, Beijing 100083, China
2 Suzhou Laboratory, Suzhou 215123, China
3 Department of Physics, School of Mathematics and Physics, University of Science and Technology Beijing, Beijing 100083, China
4 State Key Laboratory of New Ceramics and Fine Processing, School of Materials Science and Engineering, Tsinghua University, Beijing 100084, China

GRAPHICAL ABSTRACT

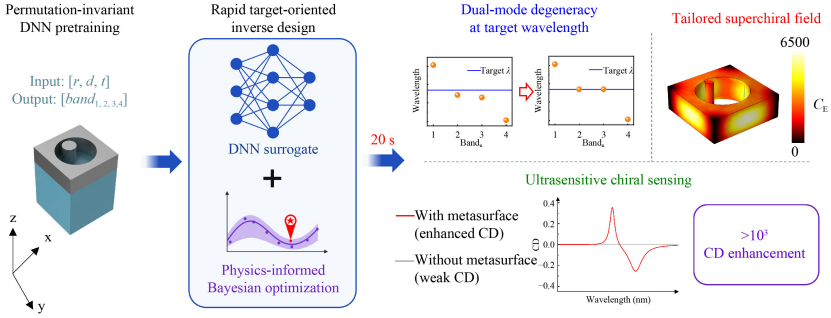

HIGHLIGHTS

- Automated inverse design of metasurfaces for tailored superchiral fields
- Deep neural network (DNN) and Bayesian optimization enable rapid, target-oriented design
- Permutation-invariant pretraining resolves mode-label switching
- Data-driven, physics-informed Bayesian optimization (BO) enables efficient constrained optimization
- Circular dichroism (CD) signals are enhanced by three orders for ultrasensitive chiral sensing

ABSTRACT Metasurfaces supporting superchiral fields provide an effective route for amplifying the intrinsically weak circular dichroism (CD) response of chiral molecules, but their design usually relies on inefficient trial-and-error optimization. Here, we propose an automated inverse-design framework that integrates a deep neural network (DNN) with Bayesian optimization (BO) for the on-demand design of metasurfaces with tailored superchiral-field responses. A high-accuracy DNN surrogate model is first trained to establish the mapping between structural parameters and eigenmodes, while a BO module performs inverse optimization through a physics-informed weighted composite objective function. To address the mode-label switching problem in modal prediction, the task is reformulated as a modal-set prediction problem and optimized using a permutation-invariant loss, which markedly improves training stability and prediction accuracy. Based on this framework, dual high-Q mode degeneracy at target wavelengths is rapidly achieved under a fixed lattice period, enabling efficient generation of customized superchiral fields. Compared with expert-guided parametric scanning, the design speed is improved by approximately 5145 times. The optimized metasurfaces provide up to 6000-fold optical chirality enhancement and yield a CD response enhanced by nearly three orders of magnitude compared to the reference without metasurfaces. This framework provides an efficient and generalizable route toward intelligent inverse design of chiral photonic devices for ultrasensitive sensing.

Received 16 April 2026; accepted 29 April 2026

E-mails: cbliu@ustb.edu.cn (Chuanbao Liu)
baiy@mater.ustb.edu.cn (Yang Bai)

* These authors contributed equally to this work.

KEYWORDS Metasurfaces; Inverse design; Deep neural networks; Bayesian optimization; Superchiral fields; Chiral sensing

1 Introduction

Chirality is a fundamental property of matter, especially playing a central role in biochemistry, pharmaceutics, and life sciences [1–3]. As an established spectroscopic tool, circular dichroism (CD) is widely used for determining the structural configuration and enantiomeric composition of chiral molecules [4–7]. However, the chiroptical response of natural molecules is intrinsically weak because their Pasteur parameters are typically very small, which imposes a major limitation on trace-level chiral detection. Enhancing chiral light–matter interactions is therefore a key challenge in the development of high-sensitivity chiral sensing technologies.

In recent years, metasurfaces have emerged as a powerful platform for boosting chiroptical responses beyond the limits of natural materials [8–10]. Owing to their subwavelength structural engineering capability, metasurfaces can support tailored resonant modes with strong local field confinement and enhanced optical chirality [11–15]. In particular, all-dielectric metasurfaces supporting quasi-bound states in the continuum (q-BICs) can simultaneously provide ultrahigh Q factors, strong light confinement, and large near-field enhancement, making them especially attractive for generating superchiral fields [16–18]. Such fields not only strengthen local chiral light–matter interactions at optical hotspots, but also provide high volume-averaged optical chirality enhancement over an extended interaction region, thereby enabling highly sensitive detection of distributed chiral molecules [16,19–21].

Despite this promise, the design of metasurfaces capable of producing strong superchiral fields at specified target wavelengths remains highly challenging. The formation of superchiral fields generally requires the coordinated fulfillment of several stringent physical conditions, including electromagnetic duality, spectral degeneracy, spatial overlap, and appropriate phase relation between the participating modes [22,23]. In practice, the underlying mapping from structural parameters to modal characteristics and eventually to chiral response is highly nonlinear, high-dimensional, and strongly coupled [24,25]. Conventional design strategies therefore rely heavily on expert intuition combined with exhaustive parametric scanning based on finite-element or finite-difference electromagnetic simulations [26]. Such approaches are not only computationally intensive, but also prone to low design efficiency and limited transferability when moving to different target wavelengths or performance requirements.

Recent great advances in deep learning have opened new opportunities for overcoming these bottlenecks in nanophotonic inverse design [27–31]. By learning from large simulation datasets, deep neural networks (DNNs) can serve as fast and accurate surrogate models for predicting optical responses, dramatically reducing the computational cost of repeated full-wave simulations [24,32–34]. However, direct inverse design based solely on generative models often suffers from limited physical controllability, insufficient robustness, and poor fabrication-awareness. A more effective strategy is therefore to combine a high-accuracy forward prediction model with a global optimization algorithm [35–37]. In this context, Bayesian optimization (BO) is particularly well suited for expensive black-box design problems, because it can efficiently balance exploration and exploitation and identify high-quality solutions with a relatively small number of evaluations [38,39].

Here, we develop a fully automated inverse-design framework that integrates a DNN-based forward predictor with BO for the on-demand design of metasurfaces supporting superchiral fields. A simulation dataset linking structural parameters to eigenmode information is first established to train a high-accuracy DNN surrogate model. To resolve the mode-label switching problem in modal prediction, the learning task is reformulated as a modal-set prediction problem and optimized using a permutation-invariant loss. On this basis, BO is employed to search the metasurface geometry through a physics-informed weighted composite objective function that jointly accounts for high-Q mode selection, target-wavelength alignment, modal degeneracy, and geometric feasibility. Using this framework, dual high-Q mode degeneracy at different target wavelengths is rapidly realized under a fixed lattice period, leading to tailored superchiral fields and markedly enhanced CD responses. This work establishes a generalized, automated design paradigm for rapidly tailoring superchiral metasurfaces for applications in ultrasensitive chiral sensing.

2 Results and Discussion

2.1 Automated inverse-design framework

An automated inverse-design framework that combines a DNN-based forward predictor with BO was developed for the on-demand design of metasurfaces supporting superchiral fields, as illustrated in Figure 1. A simulation dataset mapping structural parameters to eigenmodes was

first constructed and used for DNN pretraining, enabling rapid and accurate prediction of the resonance wavelength (λ) and quality factor (Q) of the relevant modes (Fig. 1C). Guided by the DNN predictions, BO was then employed to globally explore the structural parameter space and identify eigenmode distributions that fulfill user-defined targets (Fig. 1D and 1E). The resulting candidate structures were subsequently screened, and high-quality designs were further evaluated by simulations to quantify their chiral enhancement performance. The simulation results were iteratively fed back into the BO module to refine the probabilistic surrogate model and further focus the search on promising regions of the design space. The optimization was terminated once the performance improvement became negligible or the target design criteria were satisfied, yielding the final optimized metasurface structure (Fig. 1F).

As the model system, a dielectric metasurface consisting of periodic holes etched into a high-index slab supported on a low-index substrate was considered. The refractive indices of the slab and substrate were set to 2.4 and 1.45, respectively. The lattice period p and hole radius a were fixed at 400 and 140 nm, respectively, while the slab thickness t and cylinder radius r served as key structural parameters. To induce the transition from a bound states in the continuum (BIC) to a q-BIC, a cylindrical perturbation was introduced near the hole to break the C_2 symmetry of the structure. The cylinder was positioned along the y-axis, thereby preserving the overall mirror symmetry of the metasurface. This design ensures that the metasurface itself remains achiral, so that the measured CD signal originates entirely from the chiral molecules rather than from any intrinsic chiroptical response of the structure. The distance between the center of the cylinder and the center of the hole is defined as d. To mimic a realistic biological chiral environment, a chiral solution layer was introduced above the metasurface, with $\varepsilon_r = 2.1 + 2i \times 10^{-4}$ and $\mu_r = 1 + 2i \times 10^{-5}$. For the chiral enantiomers, the Pasteur parameter was set to $\kappa = \pm (2 + 0.4i) \times 10^{-4}$.

The DNN input vector was defined as $[r, d, t]$, providing a reduced-dimensional representation of the metasurface geometry, while the output vector was defined as $[\omega_1 - i\gamma_1, \omega_2 - i\gamma_2, \omega_3 - i\gamma_3, \omega_4 - i\gamma_4]$, corresponding to the eigenmode information of the structure. The three structural parameters considered here, slab thickness t, cylinder radius r, and cylinder position d, all play decisive roles in the formation of superchiral fields. Specifically, r and d govern the eigenmode characteristics by controlling the degree of symmetry breaking, whereas t further determines whether the two electromagnetically dual modes can achieve spectral degeneracy (Fig. S1). After pretraining, the DNN enables fast and accurate eigenmode prediction for arbitrary structural parameter sets, while the BO module iteratively assesses modal degeneracy and refines the structural parameters. Through the closed-loop strategy of "data augmentation → DNN prediction → BO-guided structural optimization → feedback-based dataset enhancement", metasurface geometries with high optical chirality enhancement are

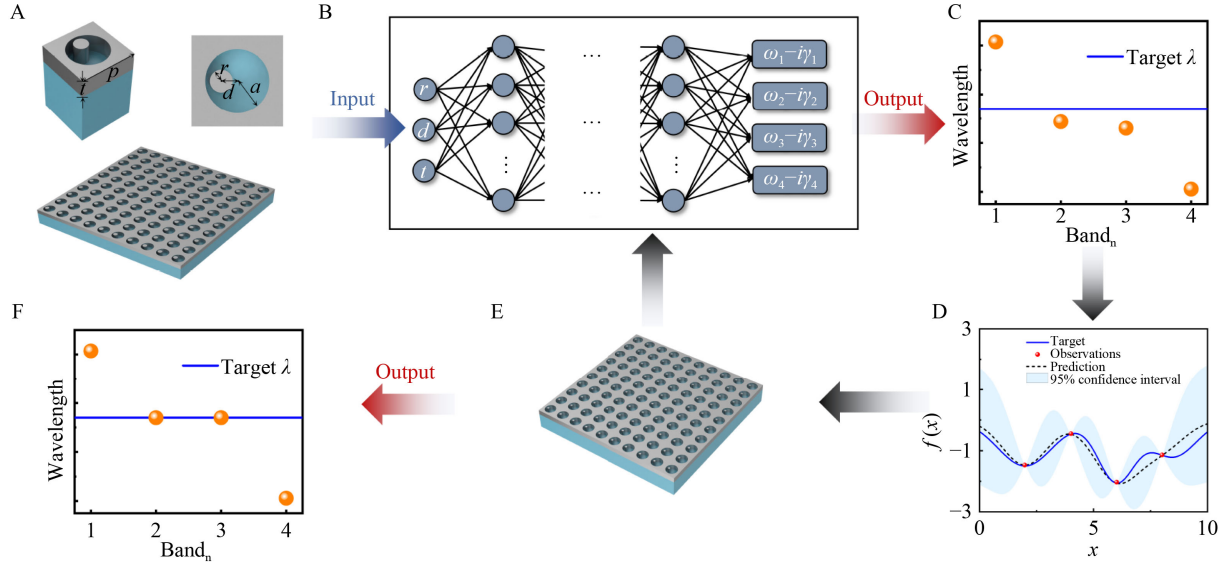

Fig. 1 Automated inverse-design framework for metasurfaces supporting superchiral fields. (A) Structural parameters of the metasurface. (B) Schematic of the DNN-based forward prediction model. (C) DNN-predicted eigenmodes of the metasurface. (D) Schematic illustration of the Bayesian optimization (BO) procedure. (E) Structural parameter combinations recommended by BO. (F) Optimized eigenmode distribution obtained through the DNN + BO framework.

progressively obtained. This framework therefore provides an efficient on-demand design platform for metasurfaces supporting superchiral fields.

2.2 DNN-based forward prediction model

A DNN-based forward prediction model was developed to learn the nonlinear correspondence between metasurface structural parameters and the corresponding eigenmodes. The model adopts a fully connected architecture consisting of an input layer, three hidden layers, and an output layer (Supporting Information note S1). The training dataset was generated using COMSOL Multiphysics software and consisted of 100,043 structural parameter combinations with their corresponding eigenmode information. The parameter ranges were defined as t = 130–140 nm, r = 5–50 nm, and d = 0–(150 − r) nm.

A critical challenge in metasurface modal prediction is mode-label switching, which is common in both modal and band-structure prediction tasks but is often overlooked. As the structural parameters vary continuously, different eigenmodes may approach, couple, cross, or undergo avoided crossing in terms of resonance wavelength, Q factor, and field distribution. As a result, the numerical ordering of a given mode is not guaranteed to remain fixed throughout the parameter space. However, in practical data-export procedures, modal outputs are usually sorted according to wavelength magnitude or eigenvalue order rather than tracked by their physical identity. Consequently, the same output column at neighboring parameter points does not necessarily correspond to the same physical mode, giving rise to label discontinuity across samples. A representative example is provided in Figure S2, where the TM_1 and TE_4 modes cross as the structural parameter r varies; although the physical mode identities remain continuous, their numerical order in the exported dataset is exchanged across the crossing point, leading directly to mode-label switching. If a conventional point-wise mean squared error (MSE) loss is directly applied, incorrect column alignment introduces artificial penalties that degrade the learning of the underlying physical mapping.

To address this issue, the original ordered multi-output regression task was reformulated as a modal-set prediction problem, in line with the general framework of permutation-invariant learning for set-structured data [40,41]. Although the input remains the same three structural parameters, the output is reformulated as an unordered set of four eigenmodes rather than a rigidly ordered modal vector, with each mode represented by its resonance wavelength and Q factor. During training, a permutation-invariant loss was introduced: all possible permutations of the four modal pairs were evaluated, and the minimum matching error was used as the optimization objective. This strategy is conceptually analogous to set-based prediction with permutation-insensitive matching [42]. In this way, the network learns the mapping from structural parameters to an unordered modal set, rather than performing element-wise regression against fixed column labels. This strategy is more consistent with the physics underlying the data-generation process and substantially improves both training stability and predictive fidelity.

To further verify the necessity of the proposed permutation-invariant modal-set learning strategy, a direct comparison was performed with a conventional ordered-label regression baseline trained using the same network architecture and dataset, but with a standard point-wise MSE loss applied to rigidly ordered modal outputs. The corresponding training and validation loss curves are shown in Figure S3. The proposed permutation-invariant model achieves stable convergence within approximately 600 epochs, whereas the conventional ordered-label regression baseline still exhibits evident overfitting even after 6000 epochs. Specifically, the ordered-label baseline exhibits a much larger discrepancy between training and validation losses, indicating that the mode-label switching problem introduces artificial supervision conflicts and severely degrades generalization. By contrast, the permutation-invariant formulation yields more stable convergence and better train-validation consistency. The final quantitative comparison is summarized in Table 1. Compared with the conventional ordered-label regression baseline, the proposed permutation-invariant modal-set learning strategy significantly reduces both the validation and test losses. In particular, the test loss is reduced by approximately 63.84%, confirming that treating the modal outputs as an unordered set effectively mitigates the error introduced by rigid label ordering and substantially improves predictive performance.

For model training, the dataset was divided into training, validation, and test sets with a ratio of 6:2:2. As shown in Figure 2A, both the training and validation losses of the DNN trained with permutation-invariant modal-set learning decrease rapidly and remain highly

Table 1 Quantitative comparison between conventional ordered-label regression and permutation-invariant modal-set learning.

Method	Train loss	Validation loss	Test loss	Test loss reduction	Relative validation-to-training loss gap
Ordered-label regression	6.50×10^{-5}	1.67×10^{-3}	1.75×10^{-3}	—	2465.54%
Permutation-invariant modal-set learning	2.80×10^{-4}	6.30×10^{-4}	6.35×10^{-4}	63.84%	125.47%

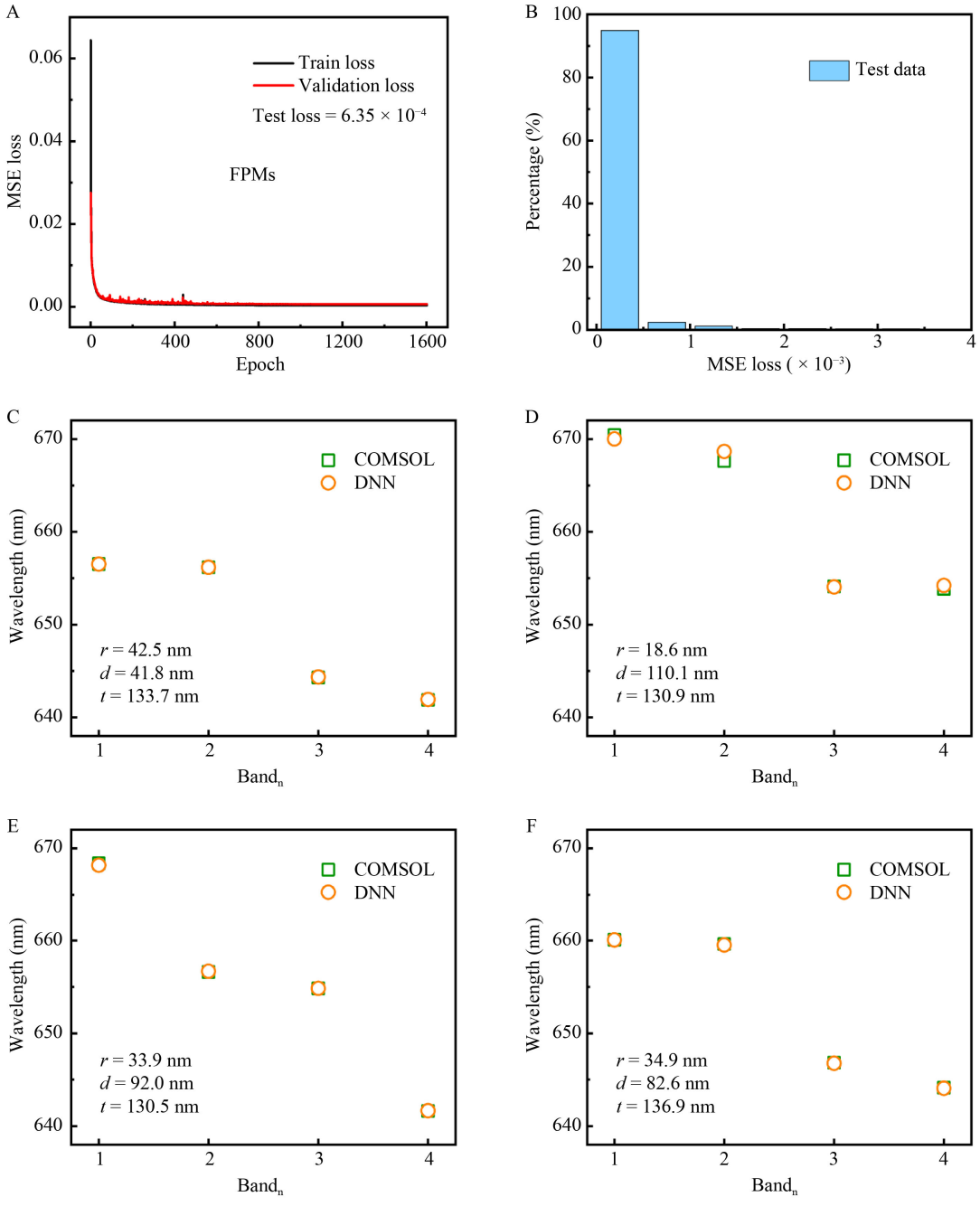

Fig. 2 Performance evaluation of the DNN-based forward prediction model. (A) Training and validation loss curves of the DNN trained with permutation-invariant modal-set learning, together with the final test loss. (B) Distribution of the test-set MSE loss. (C–F) Comparison between the DNN-predicted eigenmodes and the COMSOL-simulated eigenmodes for four randomly selected structural parameter combinations.

consistent, reaching a stable plateau after approximately 600 epochs, with no evident overfitting observed. The final test loss reaches as low as 6.35×10^{-4}, indicating excellent fitting capability and strong generalization performance.

Furthermore, the test-loss distribution shows that 94.9% of the test samples satisfy MSE $< 0.5 \times 10^{-3}$ (Fig. 2B). This level of predictive accuracy is consistent with recent deep-learning-enabled photonic inverse-design studies, in which high-fidelity surrogate models play a central role in accelerating optical-device optimization [31,34,43–45]. To further validate the predictive performance of the DNN, randomly generated structural parameter combinations were also examined. As shown in Figure 2C–F, for

four randomly selected parameter sets, the predicted eigenmodes agree closely with the COMSOL simulation results, thereby providing a reliable forward surrogate model for the subsequent BO search of structures exhibiting modal degeneracy at different target wavelengths.

2.3 Bayesian-optimization-enabled structural parameter recommendation

BO is a global optimization strategy for expensive black-box objective functions and is particularly suitable for complex photonic design problems, where the parameter space is high-dimensional, each evaluation is computationally costly, and analytical gradients are unavailable. In this work, the trained DNN served as a forward surrogate model, replacing time-consuming full-wave simulations with rapid neural-network-based prediction of the mapping between metasurface structural parameters and modal spectral responses, thereby establishing an automated DNN + BO framework for structural parameter recommendation.

Specifically, the optimization variables were chosen as the three key structural parameters of the metasurface, [r, d, t]. For any given parameter combination, the DNN efficiently predicts the resonance wavelengths and Q factors of four modes. Since the inverse-design task considered here is not a conventional label-based regression problem, but instead requires the simultaneous satisfaction of multiple physical constraints, including modal degeneracy, target-wavelength alignment, high-Q mode selection, and geometric feasibility, a weighted composite objective function was constructed, consistent with the broader idea that BO can benefit from incorporating structured physical information into the optimization target rather than relying on a purely black-box formulation [46]. First, the two modes with the highest predicted Q factors were automatically selected from the four predicted modes, and their wavelengths and Q factors were denoted as λ_1, Q_1 and λ_2, Q_2, respectively. The objective function is expressed as:

$$L_{\mathrm{BO}}=w_1L_{\mathrm{deg}}+w_2L_{\mathrm{target}}+w_3L_{\mathrm{Q-eq}}+w_4L_{\mathrm{Q-pen}}+w_5L_{\mathrm{geom}} \quad (1)$$

Here, L_{deg} denotes the modal-degeneracy term, which constrains the resonance wavelengths of the two selected high-Q modes to be as close as possible; L_{target} denotes the target-wavelength term, which constrains their average wavelength toward the preset target wavelength; $L_{\mathrm{Q\text{-}eq}}$ is the Q factor consistency term, which characterizes the similarity between the Q factors of the two selected high-Q modes; $L_{\mathrm{Q\text{-}pen}}$ is the high-Q penalty term introduced to suppress low-Q solutions; and L_{geom} is the geometric-constraint penalty term, which ensures the physical realizability of the structural parameters. The coefficients w_{i} represent the corresponding weighting factors. Through this multi-objective, weight-balanced formulation, BO is able to effectively coordinate multiple design requirements and identify candidate structures with improved overall performance. The weighting factors were introduced to encode the relative priorities of the inverse-design task rather than being treated as arbitrary fitting parameters. In the present study, the BO objective was designed to favor two high-Q modes becoming nearly degenerate around a prescribed target wavelength. Accordingly, the wavelength-degeneracy term and the target-wavelength alignment term were assigned higher priority than the auxiliary terms. In this sense, the weighting factors allow the BO process to make physically meaningful trade-offs among multiple design requirements. It should also be noted that the weighting strategy is design-objective-dependent. For example, if a stricter second-order degeneracy condition is desired, such that both the modal wavelengths and Q factors are nearly identical, then the weight associated with the Q-consistency term should be increased correspondingly.

In the three-dimensional parameter space considered in this work, even a fine-step parametric scan with only 70 discrete sampling points per parameter would lead to a total simulation burden on the order of 10^5. According to reported studies [34], even when expert knowledge is used to reduce the search space to approximately 1% of the full parameter space, about 3430 full-wave simulations are still required, corresponding to a computational cost of approximately 28.6 h, in order to obtain high-performance structures. In contrast, the automated DNN + BO parameter recommendation module proposed here typically requires only about 150 evaluations and can identify multiple satisfactory candidate parameter combinations within about 20 s, corresponding to an inverse-design speedup of approximately 5145 times. These results demonstrate that the proposed method not only substantially reduces the design cost, but also alleviates the dependence of conventional parametric scanning on expert intuition and extensive computational resources, thereby providing an efficient and generalizable route for the rapid on-demand design of complex metasurface devices.

It is worth emphasizing that the proposed DNN + BO inverse-design framework does not minimize a conventional label-based regression error. Instead, it optimizes a physics-informed weighted composite objective that jointly accounts for dual high-Q mode selection, target-wavelength alignment, modal degeneracy, and geometric feasibility, thereby enabling efficient on-demand design of superchiral fields.

2.4 Inverse design of superchiral fields

To validate the effectiveness of the proposed DNN + BO framework for the on-demand design of complex optical fields, the inverse design of superchiral fields at target wavelengths was further carried out. Unlike conventional approaches based on expert intuition and parametric scanning, the present study focuses on achieving superchiral fields at different target resonant wavelengths while maintaining the same lattice period. Since this task requires the coordinated matching of multiple modal characteristics in terms of resonant frequency, electromagnetic duality, and spatial field distribution, it is difficult to accomplish through empirical design rules alone and therefore serves as a stringent test of the inverse-design capability. The formation of superchiral fields generally relies on several key requirements: the electric and magnetic fields of two modes should satisfy electromagnetic duality; the two modes should be degenerate in frequency and strongly overlapped in space; and an appropriate phase relationship should exist between them [22]. In our structure, although the three structural parameters are varied, the overall field-profile symmetry of each mode remains essentially unchanged, while the main variations occur in field intensity and resonant position. Among all modes, the TM_1 and TE_4 q-BIC modes exhibit electromagnetic duality and strong spatial overlap (Fig. S4), and therefore define the target modal pair for superchiral-field inverse design.

In the wavelength range of interest, the DNN first predicts the resonance wavelengths and Q factors of four modes, after which the two modes with the highest Q factors are automatically selected and denoted as λ_1, Q_1 and λ_2, Q_2, respectively. Taking a target resonance wavelength of 657 nm as an example, the design objectives are defined as $y_1 = (\lambda_1 + \lambda_2)/2 - 657$, $y_2 = \lambda_1 - \lambda_2$, $y_3 = \log Q_1 - \log Q_2$. Here, y_1 constrains the average wavelength of the two selected high-Q modes toward the target value, y_2 characterizes the degree of modal degeneracy, and y_3 describes the Q factor consistency between the two modes. In addition, a high-Q penalty term and a geometric-feasibility penalty term are incorporated into the objective function to ensure that the optimized solutions remain in the high-Q regime and comply with the structural constraints.

In the practical implementation, the structural search ranges were defined as t = 130–140 nm, r = 5–50 nm, and d = 0–(150 − r) nm. During the optimization, the DNN first rapidly evaluated 100 randomly initialized structural candidates to provide an initial exploration of the parameter space. On this basis, BO was subsequently performed for 200 additional iterations, continuously proposing new structural parameter combinations and progressively approaching candidate solutions satisfying the design criteria. As shown in Figure 3A, the objective value decreased continuously as the optimization proceeded and already exhibited a clear convergence trend by the 43rd iteration. This behavior indicates that the proposed DNN + BO automated inverse-design framework can effectively capture the key modal-matching conditions required for superchiral-field generation and achieve stable convergence within a relatively small number of evaluations. To further assess the robustness of the BO stage for the representative target wavelength of 657 nm, the inverse-design process was repeated using multiple random seeds spanning the range from 0 to 10^6. As shown in Figure S5, the resulting band distributions consistently drive the two selected modes toward near-degenerate wavelengths around the target value of 657 nm. The corresponding optimized metasurface parameters and modal wavelengths are listed in Table S1. Although slight variations in the optimized structural parameters are observed across different runs, the selected modal wavelengths λ_1 and λ_2 remain consistently close to the target wavelength and nearly degenerate. The consistent BO results obtained under different random seeds further suggest that, under the present physically motivated weight setting, the inverse-design process is stable and does not rely on an accidental optimization trajectory. This result confirms that the proposed BO-based inverse-design process is robust with respect to random initialization and does not depend on a specific seed to identify high-quality solutions. Meanwhile, the framework provides not only a single optimal structure, but also multiple low-loss and mutually distinct candidate parameter combinations, thereby offering greater flexibility for subsequent device design and experimental implementation. Furthermore, under different target resonant wavelengths, the automated framework consistently achieves stable degeneracy of the TM_1 and TE_4 q-BIC modes, as shown in Figure 3B–D, thereby producing the desired superchiral-field response at the target wavelength. These results demonstrate that the proposed DNN + BO inverse-design strategy possesses excellent on-demand design capability and strong generalizability. Compared with existing superchiral-metasurface design approaches based on either manual parameter tuning or computational optimization, the present framework directly links target-wavelength-specific modal degeneracy to automated inverse design, thereby providing a more efficient route for customized superchiral-field engineering [47].

2.5 Ultrasensitive chiral sensing

The intrinsically weak CD signal of chiral molecules can be significantly enhanced by metasurfaces supporting

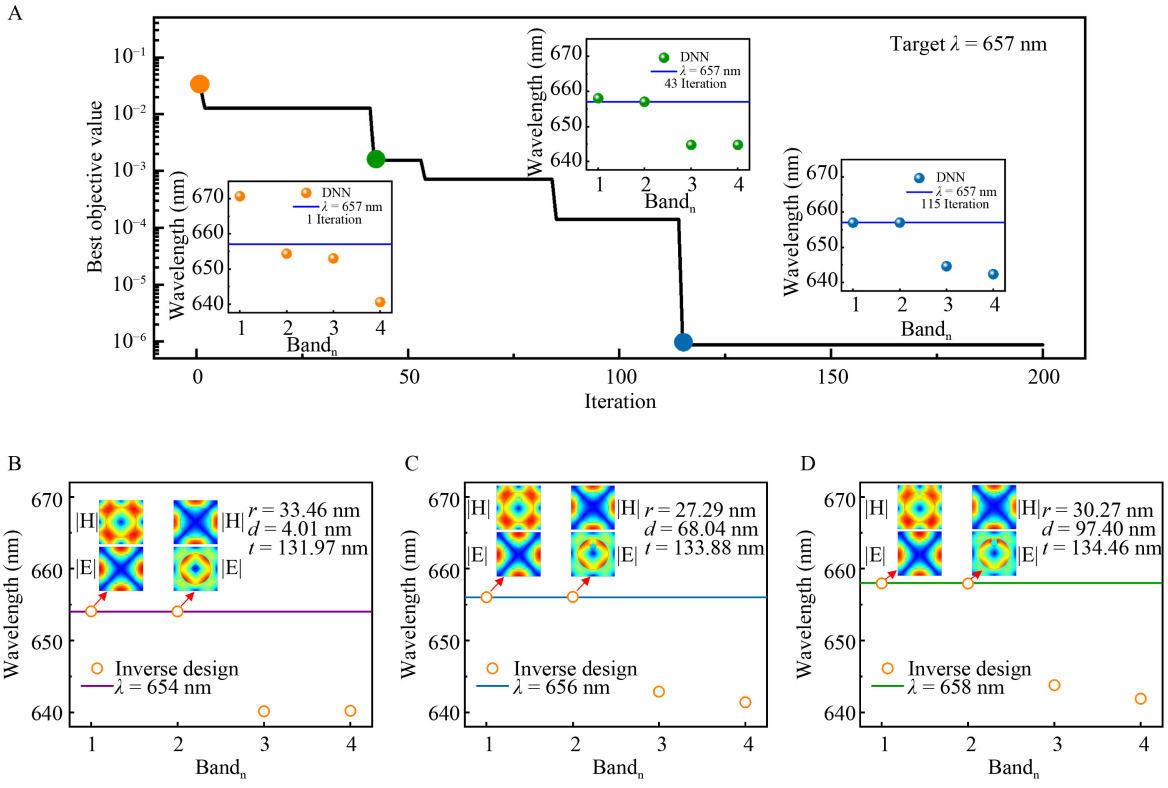

Fig. 3 Inverse design of superchiral fields using the DNN + BO framework. (A) Optimization trajectory of the BO-based inverse-design process. Inset: Evolution of the eigenmodes for three representative structural parameter sets during optimization. (B–D) Three representative inversely designed metasurface candidates exhibiting dual-mode degeneracy near the target wavelengths of (B) 654 nm, (C) 656 nm, and (D) 658 nm, respectively. Insets: Field distributions of the selected resonant modes.

strong superchiral fields, and the enhancement of the CD response is proportional to the optical chirality enhancement factor, $C_E = C/C_0$ (Supporting Information note S2). Importantly, the superchiral field formed by dual-mode degeneracy must remain helicity-preserved throughout the entire interaction volume. Otherwise, the regions with opposite signs of C_E generate the CD contributions of opposite sign, which partially cancel each other in the far field. To further evaluate the application potential of the proposed automated inverse-design framework for ultrasensitive chiral sensing, the optical chirality enhancement of the optimized structure was examined. As shown in Figure 4A, the optical chirality enhancement is positive under right-circularly polarized (RCP) incidence and negative under left-circularly polarized (LCP) incidence, indicating that a spatially uniform superchiral field can be generated near the metasurface. In addition to the strong volume-averaged optical chirality enhancement, the maximum near-field enhancement reaches up to 6000 times that of the incident circularly polarized light. The spatial distribution and large enhancement magnitude of the superchiral field therefore provide a solid basis for achieving strong chiral light–matter interactions.

Upon introducing chiral enantiomers into the solution, the system forms two hybridized branches, namely the upper branch (UB) and the lower branch (LB), exhibiting the characteristic anti-crossing behavior (Fig. S6), consistent with recent q-BIC-based studies of chiral-molecule-induced strong coupling between resonant branches [16,19]. Under the zero-detuning condition ($\lambda_1 = \lambda_2$), the Rabi splitting is calculated to be $\Omega_R = 0.165$ meV. Since this value exceeds the linewidths of both branches, $V_{UB} = 0.039$ meV and $V_{LB} = 0.110$ meV, the stringent criterion for strong coupling is satisfied. On this basis, detection of chiral enantiomers is achieved by vertically illuminating the metasurface with circularly polarized light and analyzing the corresponding absorption and CD spectra. In this work, the CD signal is defined as:

$$\mathrm{CD} = (A_{RCP} - A_{LCP})/(A_{RCP} + A_{LCP}) \quad (2)$$

where A_{RCP} and A_{LCP} denote the absorptance under RCP and LCP incidence, respectively. As shown in Figure 4B, the Rabi splitting spectrally separates the circularly polarized absorption resonances associated with A_{RCP} and A_{LCP}. Meanwhile, the loss redistribution effect further enhances the Q factor of the UB, thereby increasing its absorption intensity. As a result, the CD amplitude

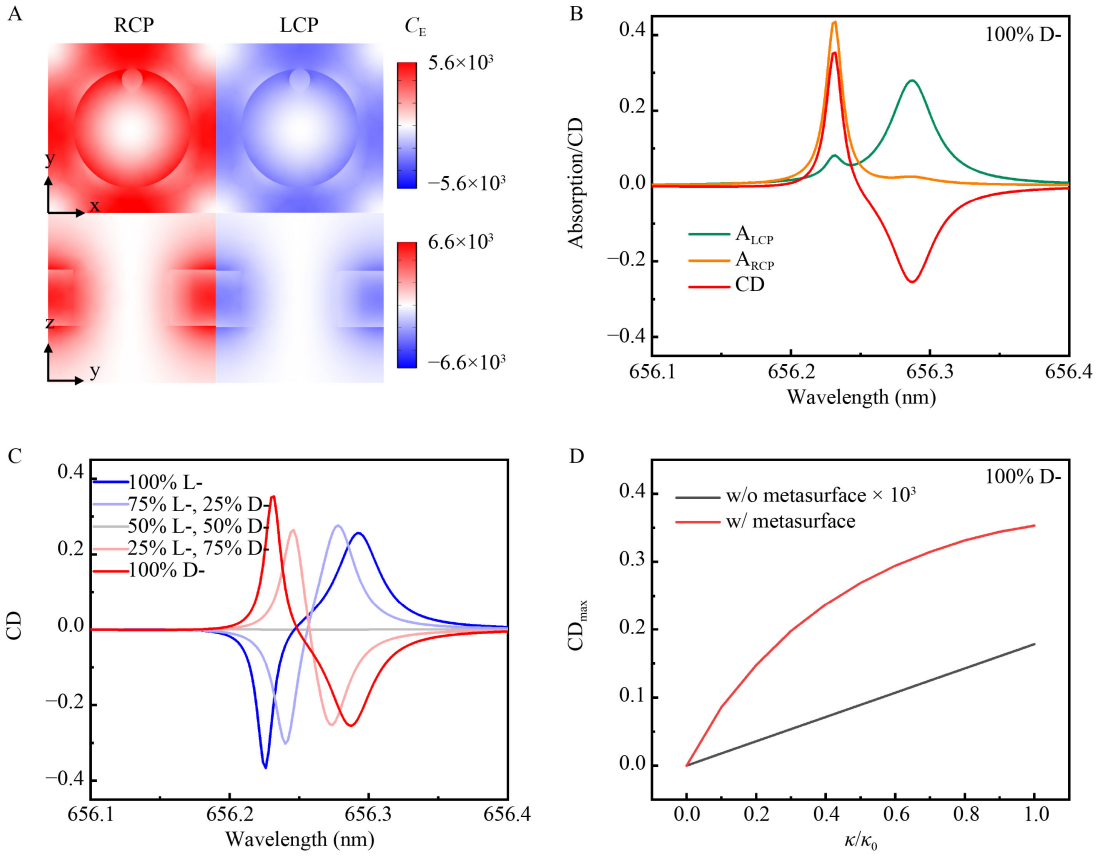

Fig. 4 Ultrasensitive chiral sensing enabled by the inversely designed metasurface. (A) Simulated distributions of the optical chirality enhancement (C_E) under RCP (left) and LCP (right) incidence. (B) Absorptance and CD spectra of a chiral sample containing 100% D-enantiomer (D-). (C) CD spectra of chiral samples containing different proportions of D- and L-enantiomers (L-). (D) Comparison of the CD response with and without the metasurface enhancement.

associated with the UB is enhanced to 0.35. Since the volume-averaged C_E of the two hybridized branches has opposite signs (Fig. S7), their corresponding CD signals also exhibit opposite signs. Furthermore, by assuming a Pasteur parameter of $\kappa = (2 + 0.4i) \times 10^{-4}$ for the D-enantiomer and $\kappa = -(2 + 0.4i) \times 10^{-4}$ for the L-enantiomer, the CD spectra of chiral samples with different enantiomeric ratios were calculated, as shown in Figure 4C. The results indicate that both the amplitude and sign of the CD spectrum can be used to characterize the composition of chiral molecules. More importantly, the metasurface supporting the superchiral field not only enables discrimination of enantiomeric ratios, but also dramatically improves the detection limit. As shown in Figure 4D, compared with the reference CD signal without the metasurface, the maximum CD response, CD_{max}, is enhanced by three orders of magnitude. This pronounced enhancement persists even at reduced filling fractions of the chiral enantiomers, highlighting the significant potential of this platform for ultrasensitive chiral sensing.

3 Conclusion

In summary, we have developed an automated inverse-design framework that combines a DNN surrogate model with BO for the rapid design of metasurfaces supporting tailored superchiral fields. By reformulating modal prediction as a modal-set learning problem and introducing a permutation-invariant loss, the framework effectively overcomes mode-label switching and achieves high prediction accuracy. Coupled with a physics-informed BO module, the method enables efficient inverse optimization of metasurface geometries under multiple design constraints. Using this strategy, dual high-Q mode degeneracy at target wavelengths is realized under a fixed lattice period, yielding strong optical chirality enhancement and markedly improved CD signals. Beyond the present dielectric metasurface platform, the proposed framework is readily extensible to other inverse-design problems in photonics and materials science, particularly those involving high-dimensional, nonlinear, and strongly coupled structure–property rela-

tionships. These results highlight the proposed framework as an efficient and generalizable platform for intelligent design of chiral photonic devices and ultrasensitive chiral sensing.

Supporting Information Supporting Information is available in the online version of this article at https://doi.org/10.2738/ENGTM.2026.0008 and is accessible for authorized users.

Data Availability The data that support the findings of this study are available from the corresponding author upon reasonable request.

Acknowledgements This work was supported by grants from the National Natural Science Foundation of China (Nos. 52325208, 52372279, 52541024, and 92463311), the Fundamental Research Funds for the Central Universities (FRF-TP-24-02C). The authors declare that no generative artificial intelligence (AI) or AI-assisted technologies were used in the preparation, analysis, or writing of this manuscript.

Competing interests All authors declared that there are no conflicts of interest.

References

1. Gong W, Chen Z, Dong J, Liu Y, Cui Y. Chiral metal–organic frameworks. Chem Rev, 2022, 122(9): 9078−9144
2. Xue Y, Cao C, Zheng Y. Enzymatic asymmetric synthesis of chiral amino acids. Chem Soc Rev, 2018, 47(4): 1516−1561
3. Kelly S A, Pohle S, Wharry S, Mix S, Allen C C R, Moody T S, Gilmore B F. Application of ω-transaminases in the pharmaceutical industry. Chem Rev, 2018, 118(1): 349−367
4. Zhou S, Bian J, Chen P, Xie M, Chao J, Hu W, Lu Y, Zhang W. Polarization-dispersive imaging spectrometer for scattering circular dichroism spectroscopy of single chiral nanostructures. Light Sci Appl, 2022, 11(1): 64
5. Daly S, Rosu F, Gabelica V. Mass-resolved electronic circular dichroism ion spectroscopy. Science, 2020, 368(6498): 1465−1468
6. Xu C, Ren Z, Zhou H, Zhou J, Ho C P, Wang N, Lee C. Expanding chiral metamaterials for retrieving fingerprints via vibrational circular dichroism. Light Sci Appl, 2023, 12(1): 154
7. Keiderling T A. Structure of condensed phase peptides: Insights from vibrational circular dichroism and raman optical activity techniques. Chem Rev, 2020, 120(7): 3381−3419
8. Han Z, Wang F, Sun J, Wang X, Tang Z. Recent advances in ultrathin chiral metasurfaces by twisted stacking. Adv Mater, 2023, 35(3): 2206141
9. Probst P T, Mayer M, Gupta V, Steiner A M, Zhou Z, Auernhammer G K, König T A F, Fery A. Mechano-tunable chiral metasurfaces via colloidal assembly. Nat Mater, 2021, 20(7): 1024−1028
10. Cen M, Wang J, Liu J, He H, Li K, Cai W, Cao T, Liu Y J. Ultrathin suspended chiral metasurfaces for enantiodiscrimination. Adv Mater, 2022, 34(37): 2203956
11. Chen Y, Deng H, Sha X, Chen W, Wang R, Chen Y-H, Wu D, Chu J, Kivshar Y S, Xiao S, Qiu C-W. Observation of intrinsic chiral bound states in the continuum. Nature, 2023, 613(7944): 474−478
12. Zhang X, Liu Y, Han J, Kivshar Y, Song Q. Chiral emission from resonant metasurfaces. Science, 2022, 377(6611): 1215−1218
13. Gorkunov M V, Antonov A A, Kivshar Y S. Metasurfaces with maximum chirality empowered by bound states in the continuum. Phys Rev Lett, 2020, 125(9): 093903
14. Overvig A, Yu N, Alù A. Chiral quasi-bound states in the continuum. Phys Rev Lett, 2021, 126(7): 073001
15. Lim Y, Seo I C, An S-C, Kim Y, Park C, Woo B H, Kim S, Park H-R, Jun Y C. Maximally chiral emission via chiral quasibound states in the continuum. Laser Photonics Rev, 2023, 17(2): 2200611
16. Chen Y, Chen W, Kong X, Wu D, Chu J, Qiu C-W. Can weak chirality induce strong coupling between resonant states? Phys Rev Lett, 2022, 128(14): 146102
17. Kang M, Liu T, Chan C T, Xiao M. Applications of bound states in the continuum in photonics. Nat Rev Phys, 2023, 5(11): 659−678
18. Hsu C W, Zhen B, Stone A D, Joannopoulos J D, Soljačić M. Bound states in the continuum. Nat Rev Mater, 2016, 1(9): 16048
19. Guan T, Wang Z, Wang R, Wu Z, Wang C, Wu D, Chu J, Chen Y. Ultrasensitive circular dichroism spectroscopy based on coupled quasi-bound states in the continuum. Nanophotonics, 2025, 14(8): 1083−1089
20. Jin R, Zhang X, Huo P, Cai Z, Lu Y, Xu T, Liu Y. Harnessing enantioselective optical forces by quasibound states in the continuum. Phys Rev Lett, 2024, 133(8): 086901
21. Zhang X, Wang C, Jin R, Dong Z, Kivshar Y, Liu Y. Enhancing superchiral fields and circular dichroism detection with achiral dielectric metasurfaces. Nano Lett, 2025, 25(33): 12620−12626
22. Ye L, Li J, Richter F U, Jahani Y, Lu R, Lee B R, Tseng M L, Altug H. Dielectric tetramer nanoresonators supporting strong superchiral fields for vibrational circular dichroism spectroscopy. ACS Photonics, 2023, 10(12): 4377−4384
23. Solomon M L, Hu J, Lawrence M, García-Etxarri A, Dionne J A. Enantiospecific optical enhancement of chiral sensing and separation with dielectric metasurfaces. ACS Photonics, 2019, 6(1): 43−49
24. Jiang J, Chen M, Fan J A. Deep neural networks for the evaluation and design of photonic devices. Nat Rev Mater, 2021, 6(8): 679−700
25. Li Z, Pestourie R, Lin Z, Johnson S G, Capasso F. Empowering metasurfaces with inverse design: Principles and applications. ACS Photonics, 2022, 9(7): 2178−2192
26. Arbabi A, Horie Y, Bagheri M, Faraon A. Dielectric metasurfaces for complete control of phase and polarization with subwavelength spatial resolution and high transmission. Nat Nanotechnol, 2015, 10(11): 937−943
27. Ma W, Liu Z, Kudyshev Z A, Boltasseva A, Cai W, Liu Y. Deep learning for the design of photonic structures. Nat Photonics, 2021, 15(2): 77−90
28. Zhang N, Gao F, Wang R, Shen Z, Han D, Cui Y, Zhang L,

Chang C, Qiu C-W, Chen X. Deep-learning empowered customized chiral metasurface for calibration-free biosensing. Adv Mater, 2025, 37(1): 2411490

29. Wang J, Yao B, Niu Y, Ma J, Wang Y, Qu Z, Duan J, Zhang B. Generative adversarial networks for high degree of freedom metasurface designs. Advanced Composites and Hybrid Materials, 2024, 8(1): 94
30. Yin Y, Jiang Q, Wang H, Liu J, Xie Y, Wang Q, Wang Y, Huang L. Multi-dimensional multiplexed metasurface holography by inverse design. Adv Mater, 2024, 36(21): 2312303
31. Ma W, Cheng F, Liu Y. Deep-learning-enabled on-demand design of chiral metamaterials. ACS Nano, 2018, 12(6): 6326−6334
32. Qian C, Kaminer I, Chen H. A guidance to intelligent metamaterials and metamaterials intelligence. Nature Commun, 2025, 16(1): 1154
33. Chen M K, Liu X, Sun Y, Tsai D P. Artificial intelligence in meta-optics. Chem Rev, 2022, 122(19): 15356−15413
34. An S, Fowler C, Zheng B, Shalaginov M Y, Tang H, Li H, Zhou L, Ding J, Agarwal A M, Rivero-Baleine C, Richardson K A, Gu T, Hu J, Zhang H. A deep learning approach for objective-driven all-dielectric metasurface design. ACS Photonics, 2019, 6(12): 3196−3207
35. Wang S, Yang Y. Metasurface designed with quantitative field distributions. Light Sci Appl, 2023, 12(1): 114
36. Wang M, Bao Y, Wang W, Li N, Hu X, Chu T, Ying Y, Xu W, Xiong B, Ma W. A hybrid algorithm-driven approach for efficient design of terahertz molecule-specific metasensors. Chip, 2026, 5(1): 100162
37. Zhu D, Liu Z, Raju L, Kim A S, Cai W. Building multifunctional metasystems via algorithmic construction. ACS Nano, 2021, 15(2): 2318−2326
38. Li Y, Xu Y, Jiang M, Li B, Han T, Chi C, Lin F, Shen B, Zhu X, Lai L, Fang Z. Self-learning perfect optical chirality via a deep neural network. Phys Rev Lett, 2019, 123(21): 213902
39. Tao C, Liu C, Li Y, Qian S, Han W, Wang F, Zhao S, Ren F, Bai Y, Li B, Zhou J. Tailoring the optical transfer function of nonlocal metasurfaces for targeted image processing via an automated inverse design framework. Microstructures, 2026, 6(2): 2026035
40. Zaheer M, Kottur S, Ravanbhakhsh S, Póczos B, Salakhutdinov R, Smola A J. Deep sets. In: *Adv Neural Inform Process Syst*, 2017, 3394–3404
41. Lee J, Lee Y, Kim J, Kosiorek A, Choi S, Teh Y W. Set transformer: A framework for attention-based permutation-invariant neural networks. In: Proc Int Conf Mach Learn, 2019, 3744–3753
42. Carion N, Massa F, Synnaeve G, Usunier N, Kirillov A, Zagoruyko S. End-to-end object detection with transformers. In: Proc Eur Conf Comput Vis, 2020, 213−229
43. Malkiel I, Mrejen M, Nagler A, Arieli U, Wolf L, Suchowski H. Plasmonic nanostructure design and characterization via deep learning. Light Sci Appl, 2018, 7(1): 60
44. Li Z, Xu J, Zhang L, Li Y, Yang R, Fu Q, Zhang F, Fan Y. Inverse design of dual-band optically transparent metasurface absorbers with neural-adjoint method. Ann Phys, 2023, 535(6): 2300054
45. Xu B, Shao J, Zhao X, Xu H, Tian Y, Chen N, Sun J, Lin H, Bao Q, Mai Y, Wu C. Deep-learning-enabled inverse design of large-scale metasurfaces with full-wave accuracy. Laser Photonics Rev, 2026, 20(5): e03115
46. Astudillo R, Frazier P I. Thinking inside the box: A tutorial on grey-box bayesian optimization. In: Proc Winter Simul Conf, 2022, Article 2
47. Jiang Z, Sohag S H, Zhou Y. Near-field topology-optimized superchiral metasurfaces for enhanced chiral sensing. Nano Lett, 2026, 26(3): 1109−1117